

# Differentiable Cosmological Hydrodynamics for Field-Level Inference and High Dimensional Parameter Constraints

Benjamin Horowitz<sup>1,2,3</sup>★ and Zarija Lukić<sup>3</sup>

<sup>1</sup>*Kavli IPMU (WPI), UTIAS, The University of Tokyo, Kashiwa, Chiba 277-8583, Japan*

<sup>2</sup>*Center for Data-Driven Discovery, Kavli IPMU (WPI), UTIAS, The University of Tokyo, Kashiwa, Chiba 277-8583, Japan*

<sup>3</sup>*Lawrence Berkeley National Lab, 1 Cyclotron Road, Berkeley, CA 94720, USA*

January 2025

## ABSTRACT

Hydrodynamical simulations are the most accurate way to model structure formation in the universe, but they often involve a large number of astrophysical parameters modeling subgrid physics, in addition to cosmological parameters. This results in a high-dimensional space that is difficult to jointly constrain using traditional statistical methods due to prohibitive computational costs. To address this, we present a fully differentiable approach for cosmological hydrodynamical simulations and a proof-of-concept implementation, `diffHydro`. By back-propagating through an upwind finite volume scheme for solving the Euler Equations jointly with a dark matter particle-mesh method for Poisson equation, we are able to efficiently evaluate derivatives of the output baryonic fields with respect to input density and model parameters. Importantly, we demonstrate how to differentiate through stochastically sampled discrete random variables, which frequently appear in subgrid models. We use this framework to rapidly sample sub-grid physics and cosmological parameters as well as perform field level inference of initial conditions using high dimensional optimization techniques. Our code is implemented in JAX (python), allowing easy code development and GPU acceleration.

**Key words:** methods: numerical

## 1 INTRODUCTION

A core goal of modern cosmology is to understand the formation of the large scale structure of the universe and trace its evolution over cosmic time. However, most of the mass-energy density of the universe is found in the dark sector (i.e. dark matter and energy) and we are left interpreting its impact on baryons as biased tracers of this underlying distribution. This presents major theoretical and practical challenges to calculate and propagate uncertainties to constrain cosmological models.

A key tool for modeling the baryons together with the dark sector is cosmological hydrodynamical simulations (Cen 1992). While the dark matter can be modeled as a collisionless fluid via pure gravitational dynamics, baryonic gas is collisional and therefore requires solving the compressible Euler fluid equations. In addition, small-scale astrophysical phenomena, such as star formation and AGN activity (Dimonte & Tipton 2006; Robertson & Kravtsov 2008; Rahimi & Kawata 2012; Teyssier et al. 2013; Oku et al. 2022; Oku & Nagamine 2024) operate on scales not directly resolvable in large-scale cosmological simulations, “subgrid” models approximate their influence on the larger, resolved structures. Jointly solving this evolution is computationally demanding and requires the introduction of additional modeling parameters beyond the cosmological model itself. Relevant summary statistics are then calculated from outputs of these hydrodynamical simulations and compared to the observational data from sky surveys (Kugel et al. 2023).

However, a full likelihood analysis requires exploration of the entire parameter space of cosmological models. This usually entails running many hydrodynamical simulations sampling a model parameter space, with either summary statistics interpolated in this space (e.g. power spectra emulators Heitmann et al. 2010; Walther et al. 2019; Giri & Schneider 2021) or a machine learning-based augmentation (Horowitz et al. 2019b; Harrington et al. 2022; Sharma et al. 2024). Depending on the dimensionality of the parameter space and the cosmic volumes under consideration, this can be extremely expensive computationally. To simplify this, many astrophysical parameters are fixed via manual calibration via various astrophysical observables (i.e. galaxy luminosity functions,  $M-M_*$  relations, etc.), many of which also have some cosmological dependencies (Weinberger et al. 2017).

In recent years, there has also been an increased interest in moving beyond summary statistics and to use field level inference for cosmological constraints and cosmic structure inference (Jasche & Wandelt 2013; Seljak et al. 2017; Ata et al. 2022; Nguyen et al. 2024). These methods use full forward modeling from the initial conditions of the universe to the late time observable field to then compare with data. This requires performing a high dimensional optimization and/or sampling algorithm, relying on derivative back-propagation through the dynamical model (Seljak et al. 2017; Li et al. 2022). Perturbation and particle mesh methods for gravity evolution can be differentiated straightforwardly, and then mapped to the the observable signal via bias models (e.g. Horowitz et al. 2019a, 2021).

Uncertainties in this mapping, however, significantly limit the constraining power. For example, there are dense proto-clusters at  $z \sim 2.3$

★ E-mail: ben.horowitz@ipmu.jp

with similar galaxy number densities but vastly different Lyman- $\alpha$  forest statistics (Dong et al. 2023, 2024) in ways that are difficult for analytical prescriptions to capture (Kooistra et al. 2022). One approach to these modeling issues is by emulation of the baryonic fields via machine learning algorithms (Modi et al. 2018; Harrington et al. 2022; Horowitz et al. 2022). In this way, a model is trained based on simulations to map from a dark matter field to the baryon fields of interest. However, this relies on calibration against a large set of simulations spanning both cosmological and astrophysical parameters. A full analysis may involve tens if not hundreds of parameters, requiring a prohibitively large number of simulations to span the plausible parameter space and train an emulator.

In this work, we present an alternative approach; we make the hydrodynamical simulation itself differentiable with respect to the initial conditions and parameters, both cosmological and stochastic astrophysical. This enables a wide range of analysis that are otherwise impossible. This includes; rapid tuning of sub-grid physics parameters, joint calibration of astrophysical and cosmological parameter from observed summary statistics, and field level inference of hydrodynamical fields/related observables.

By leveraging existing automatic differentiation machinery developed for deep neural networks (Maddison et al. 2016; Bradbury et al. 2021), our implementation has comparable computational cost and memory usage as a standard GPU-accelerated hydrodynamical simulation or large machine learning model. We emphasize, however, that there is no emulation or calibration within this method and we directly solve for all physics as described below. In addition, our implementation is based on the JAX framework, which utilizes Just-In-Time compilation, enabling extremely fast function evaluations on a GPU. JAX has been used for differentiable simulations in a wide range of physical simulations outside astrophysics, including Boltzmann lattice models for fluids (Ataei & Salehipour 2024) and plasma physics in tokamak reactors (Citrin et al. 2024). Our software, `diffHydro` retains high user-readability, allowing rapid development and a useful test-bed for new numerical routines, subgrid prescriptions, and observed fields.

For forward modeling gas dynamics, we implement a total variation diminishing (TVD) method for solving Euler equations. TVD methods are widely used for solving the Euler equations as they effectively capture shock waves and discontinuities while minimizing unphysical oscillations. These methods offer high-resolution solutions in smooth regions and maintain numerical stability due to their ability to limit total variation (Shu 1988; Harten 1997). They also conserve mass, momentum, and energy, which is essential for accurate fluid flow simulations (LeVeque 2002). While they perform well with shocks, they are less effective at handling contact discontinuities and may introduce over-dissipation, reducing the sharpness of shock waves (Laney 1998).

We want to emphasize that modern cosmological hydrodynamical simulations (e.g. Genel et al. 2014; Schneider & Robertson 2015) employ complex numerical methods and our implementation is a proof of principle. While we demonstrate the key components of differentiable hydrodynamical simulations and how they can be used for field-level inference or to constrain parameters of interest, more development is needed to apply these methods at scale for ongoing and upcoming cosmological surveys.

## 2 METHODS

In this section, we briefly describe the equations we use to solve the underlying gas and dark matter evolution in `diffHydro`.

We are particularly focused on a formalism that is differentiable; i.e. we want to be able calculate derivatives of the resulting simulation fields, i.e. density, internal energy, velocity, etc., with respect to both the model parameters, such as cosmological parameters, as well as the initial conditions of the simulations. If this is computationally tractable, we can further calculate statistics, such as power spectra, from those fields and use the chain-rule to calculate the derivative of those statistics with respect to the astrophysical/cosmological parameters and initial conditions.

### 2.1 Initial Conditions

To set our initial conditions, we use the Einstein and Hu fitting formula for the matter transfer function (Eisenstein & Hu 1999, 1998) as implemented in the JAX-COSMO package (Campagne et al. 2023). Since this formula is analytic, we can differentiate our model with respect to cosmological parameters and deviations from this model are not expected to be significant at scales of interest for our analysis. We then use LPT to evolve the initial gaussian realization to  $z = 99$  to set our initial conditions for the full hydrodynamical simulation.

An alternative approach is to take the underlying Boltzmann codes (i.e. CLASS (Lesgourgues 2011) or CAMB (Lewis & Challinor 2011)) and make it differentiable. This could be done either by direct backpropagation through the solver (Hahn et al. 2024; Li et al. 2023) or via precomputed emulation (Aricò et al. 2023). The relative importance of the full treatment depends on the end application.

### 2.2 Dark Matter

Current cosmological constraints (Planck Collaboration et al. 2020) indicate that the matter content of the universe is dominated by a non-relativistic, pressure-less fluid known as cold dark matter. The evolution of the phase space distribution function,  $f$ , of this fluid in an expanding space-time can be described by the Vlasov equations,

$$\frac{\partial f}{\partial t} + \frac{1}{ma^2} \mathbf{p} \cdot \nabla f - m \nabla \phi \cdot \frac{\partial f}{\partial \mathbf{p}} = 0, \quad (1)$$

where  $a$  is the cosmological scale factor,  $\mathbf{p}$  is the momenta,  $m$  is the particle mass, and  $\phi$  is the gravitational potential. In practice solving this as a continuum equation is impractical in the cosmological context and instead the common approach is to monte carlo sample it at some initial time. We then evolve the discrete particles as an N-body system. Hamilton's equations for this system become

$$\frac{d\mathbf{x}_i}{dt} = \frac{1}{a} \mathbf{u}_i \quad (2)$$

$$\frac{d(a\mathbf{u}_i)}{dt} = \mathbf{g}_i \quad (3)$$

where  $\mathbf{x}(\mathbf{u})$  is the comoving location (peculiar velocity) for  $i$ th particle and  $\mathbf{g}_i$  is the gravitational field evaluated at  $\mathbf{x}_i$  at time  $t$ .

The dark matter evolution requires special care in order to allow easy propagation of gradient information. Standard N-body codes that rely on calculating particle-particle interactions described in Eq. 2 on small scales, (see, for example Springel et al. 2001; Bagla 2002; Habib et al. 2016) rely on constructing large tree structures (Barnes & Hut 1986) for calculating forces on particles in a computationally efficient way. However these structures pose significant challenges for back-propagation due to the discrete assignment into the tree structure. In particular, tree-based methods are generally piece-wise constant and therefore their derivatives are zero almost everywhere. While certain graph theory algorithms can be made differentiable (Berthet et al. 2020), the memory requirements for these approaches

generally scale poorly with particle number. In addition, for the application of field level inference, actual reconstruction of individual particle orbits (i.e. in virialized systems) is likely both unnecessary for cosmological observables and unwanted due to the introduction of significant posterior degeneracies due to chaotic orbits.

Instead we utilize a particle-mesh scheme (Hockney & Eastwood 1988; Couchman 1991), in particular a JAX implementation (Lanzieri et al. 2022) of a fast particle mesh solver (Feng et al. 2016), which utilizes a modified kick-drift-kick scheme for particle evolution (Quinn et al. 1997). As forces are calculated via a potential formalism, we are able to do calculations on a grid with standard linear algebra and Fourier operators. This allows straight-forward backpropagation via automatic differentiation.

We note that using a Particle Mesh scheme without adaptive refinement fundamentally limits ability to resolve small scale dark matter structures. Depending on the physics of interest, this may pose a fundamental limitation in the ability of this particular approach. Certain techniques, including Neural-ODE solvers for integration (Lanzieri et al. 2022, 2023; Payot et al. 2023) or potential gradient descent methods (Dai et al. 2018), have been demonstrated to improve results and significantly reduce differences between PM and full N-body algorithms.

### 2.3 Gas Physics

We solve Euler equations of gasdynamics in a coordinate systems comoving with the cosmological expansion. Comoving density and pressure of the gas are related to the proper density via the cosmological scale factor,  $a$ , as  $\rho_b = a^3 \rho_{\text{prop}}$  and  $p_b = a^3 p_{\text{prop}}$ . We can then write the continuity and momentum equation for the comoving density/pressure in terms of peculiar baryon velocity,  $U$ , as

$$\frac{\partial \rho_b}{\partial t} = -\frac{1}{a} \nabla \cdot (\rho_b U), \quad (4)$$

$$\frac{\partial (a \rho_b U)}{\partial t} = -\nabla \cdot (\rho_b U U) - \nabla p + \rho_b \mathbf{g}, \quad (5)$$

where the gravitational acceleration is defined as  $\mathbf{g} = -\nabla \phi$ , where  $\phi$  is the gravitational potential.

For now, we use a single energy formalism where we keep track of the total energy,  $E$ , in each cell, which can be related to the internal energy,  $e$ , as  $E = e + \frac{1}{2} U^2$ . This can straightforwardly be expanded to a dual energy formalism, bringing more accurate solutions in low-density, high-velocity regions of the flow. The evolution of the total energy is given as;

$$\frac{\partial (a^2 \rho_b E)}{\partial t} = -a \nabla \cdot (\rho_b U E + p U) + a \rho_b U \cdot \mathbf{g} + a \dot{a} ((2-3(\gamma-2)) \rho_b e). \quad (6)$$

Baryonic matter is generally assumed to follow a power-law equation of state of the form  $p_b = (\gamma - 1) \rho_b e$ , with  $\gamma = 5/3$ . This allows us to simplify the total evolution evolution as

$$\frac{\partial (a^2 \rho_b E)}{\partial t} = -a \nabla \cdot (\rho_b U E + p U) + a (\rho_b U \cdot \mathbf{g}), \quad (7)$$

We note that there is often a heating/cooling term as well,  $\Lambda_{HC}$ , which we are not including in this work in order to better elucidate our simulations performance without confounding factors. This term is straightforward to include in our framework via a pre-computed lookup table.

More generally, we can re-express Equations 4, 5, and 7 in vector form in terms of  $\mathbf{U} = (\rho_b, a \rho_b U_x, a \rho_b U_y, a \rho_b U_z, a^2 \rho_b E) =$

$(\rho_b, a \rho_b U, a^2 \rho_b E)$ , via the following combined conservation equation,

$$\frac{\partial \mathbf{U}}{\partial t} = -\nabla \cdot \mathbf{F} + S_e + S_g, \quad (8)$$

where our flux vector is  $\mathbf{F} = ((1/a) \rho_b U, \rho_b U U, a (\rho_b U E + p U))$ , the internal energy evolution source is  $S_e = (0, 0, -a p \nabla \cdot U)$ , and the gravitational source term is  $S_g = (0, \rho_b \mathbf{g}, a \rho_b U \cdot \mathbf{g})$ .

#### 2.3.1 Relaxed Total Variation Diminishing Method

We solve these equations on a fixed grid, with our state vector  $\mathbf{U}$  defined in the center of each grid cell and our fluxes defined on the boundaries between cells. We use a relaxation method (Jin & Xin 1995), which has been shown to be effective at resolving astrophysical shocks (Pen 1998). This approach follows the procedure described in Trac & Pen (2003).

In one dimension, we can adopt a symmetric approach to general advection by decomposing our state vector into a left moving and right moving flow, i.e.

$$\mathbf{U}^R = \left( \frac{1 + v/|v|}{2} \right) \mathbf{U}, \quad (9)$$

$$\mathbf{U}^L = \left( \frac{1 - v/|v|}{2} \right) \mathbf{U}. \quad (10)$$

We can rewrite Eq. 8 in terms of the left and right moving fluxes as

$$\frac{\partial \mathbf{U}}{\partial t} + \frac{\partial \mathbf{F}^R}{\partial t} - \frac{\partial \mathbf{F}^L}{\partial t} = 0, \quad (11)$$

where the fluxes are defined as  $\mathbf{F}^i = c \mathbf{U}^i$  where  $c = |v| + c_s$  is the ‘‘freezing speed’’ with  $c_s$  the speed of sound at the current point in space.

We solve this equation using a second-order Runge-Kutta time integration scheme. The first half-step we update our state vector at time  $t$  and cell  $n$  as

$$\mathbf{U}_n^{t+\Delta t/2} = \mathbf{U}_n^t - \left( \frac{\mathbf{F}_{n+1/2}^t - \mathbf{F}_{n-1/2}^t}{\Delta x} \right) \frac{\Delta t}{2}, \quad (12)$$

where we define our fluxes at each cell boundary as  $\mathbf{F}_{n+1/2}^t = \mathbf{F}_{n+1/2}^{R,t} - \mathbf{F}_{n+1/2}^{L,t}$ . We then recalculate the boundary fluxes, i.e.  $\mathbf{F}_n^{t+\Delta t/2}$ , and perform a full time step as

$$\mathbf{U}_n^{t+\Delta t} = \mathbf{U}_n^{t+\Delta t/2} - \left( \frac{\mathbf{F}_{n+1/2}^{t+\Delta t/2} - \mathbf{F}_{n-1/2}^{t+\Delta t/2}}{\Delta x} \right) \Delta t. \quad (13)$$

#### 2.3.2 Calculating Boundary Fluxes to Second Order

In order to evaluate the terms in Eq. 12 and 13, we need to calculate the fluxes at cell boundaries based on those at cell centers. For this we use a second order upwinding scheme which has been demonstrated to be stable and able to capture complex phenomena like astrophysical shocks. To first order we can describe the flux at the right boundary of cell  $n$  as,

$$\mathbf{F}_{n+1/2}^t = \begin{cases} \mathbf{F}_n^t & v > 0 \\ \mathbf{F}_{n+1}^t & v \leq 0 \end{cases} \quad (14)$$

While the first order scheme is conservative and doesn’t produce spurious oscillations, it is highly diffusive. To this we add a nonlinear

second-order accurate total variation diminishing (TVD) scheme on top of the standard first order upwinding, for the left and right moving waves,

$$\Delta \mathbf{F}_{n+1/2}^{L,t} = \frac{\mathbf{F}_n^t - \mathbf{F}_{n-1}^t}{2} \quad (15)$$

$$\Delta \mathbf{F}_{n+1/2}^{R,t} = \frac{\mathbf{F}_{n+1}^t - \mathbf{F}_n^t}{2} \quad (16)$$

The correct second order correction depends on the the direction of flow and we therefore use a flux limiter,  $\phi$ , to determine which second order approximation is appropriate (Hirsch 1990), i.e.

$$\Delta \mathbf{F}_{n+1/2} = \phi(\Delta \mathbf{F}_{n+1/2}^{L,t}, \Delta \mathbf{F}_{n+1/2}^{R,t}). \quad (17)$$

It is important to note that certain common choices for the TVD flux limiter (such as the “minmod” limiter) would be difficult to implement differentiable due to discrete changes in sign that could lead to vanishing derivatives and poor performance in downstream inference tasks. We instead use an altered Van Leer limiter (Van Leer 1974) which uses the harmonic mean between the left and right corrections

$$\text{vanleer}(a, b) = \frac{2ab}{a + b + \epsilon}, \quad (18)$$

where  $\epsilon$  is a small correction to maintain analytical derivatives near  $a = b = 0$ .

To go to three dimensions, we can follow the the Strang splitting scheme (Strang 1968), wherein we solve each direction sequentially and for the next timestep we reverse the order, permuting the dimensions every other timestep (i.e. XYZZYX, ZXYXZ, YZXXZY). This splitting scheme has a number of computational/implementation advantages, as each direction is a combination of linear operators and is straightforward to differentiate. In addition, within the JAX environment, we can compile this the dimensional relaxation operator as a function of dimension allowing rapid evaluation on GPU.

### 2.3.3 Time-stepping

A critical choice for any simulation is how to choose a time-step. We do not implement any time-subcycling and use global time-steps. There are a two main time scales of interest, the dark matter gravitational timescale and the hydrodynamical timescale. In practice, since we are using particle mesh dynamics for the dark matter, we do not resolve virialization of the dark matter particles and velocities stay comparatively small. This results in a comparatively long timescale throughout the simulation run.

To inform our choice of timestep from the hydrodynamical physics, we use the CFL (Courant-Friedrichs-Lewy) condition. It essentially states that information cannot propagate numerically faster than the underlying physics would allow. In practical terms, a fluid element should not travel more than one grid cell during one timestep. This is expressed mathematically as the CFL coefficient  $C$ , where:

$$C = \frac{v\Delta t}{\Delta x} \leq C_{max}. \quad (19)$$

Here,  $v$  is the characteristic velocity (which could be the fluid velocity, sound speed, or any other relevant wave speed),  $\Delta t$  is the timestep, and  $\Delta x$  is the grid spacing. Typically,  $C_{max}$  is set to  $\leq 1$  for explicit time integration schemes, and in practice, values of 0.2-0.5 are often used for good accuracy and stability margin. In our case, extra care needs to be taken in choice of this number since ensuring solution accuracy is not sufficient for ensuring derivative stability. For most applications,

including parameter inference within HMC, noisy gradients can be tolerated up to a point. While there does exist some theoretical work on how to best control this noise (Chen et al. 2014), in practice we can test our gradients before the inference step.

For hydrodynamical simulations, one must consider all relevant wave speeds. In the case of compressible flow, such as for cosmic baryons, this means taking into account both the bulk fluid velocity and the sound speed. The timestep must satisfy the CFL condition for the maximum wave speed:

$$\Delta t \leq \frac{(C_{max}\Delta x)}{|v| + c_s}, \quad (20)$$

where  $c_s$  is the local sound speed. This ensures that acoustic waves, shocks, and gas advection are all properly resolved in the numerical solution.

Depending on application, care needs to be taken in how the number of iterations and choice of time-step is chosen in order to get to the target redshift. While one can back-propagate through our timestep calculation and enforce that the total integrated time results in the target redshift, in practice it simpler to predefine our time-stepping scheme even if it might mean excessive iterations. For constructing differentiable summary statistics, this is a fairly natural choice as one can use the first simulation to establish the time-step schedule. Significant deviations from the fiducial model may require readjusting the time-step schedule; i.e. if structure forms at a significantly different redshift where the time-steps are too large numerical accuracy will be lost.

Time-step accuracy can be checked explicitly by calculating  $\Delta t$  with Eq. 20 for each time-step of the solution simulation and comparing it to that of the fiducial model. Since a comparatively small  $C_{max}$  is used for the fiducial model only require a condition that  $\Delta t_{i,\text{fid}}/\Delta t_{i,\text{sol}} \leq C_{\text{fid}}/C_{\text{forward}}$  for all time-steps  $i$ , where  $C_{\text{forward}}$  is the maximum CFL number which still holds numerical accuracy on the forward pass ignoring accuracy of derivative calculations.  $C_{\text{forward}}$  can be found via standard convergence analysis, and in our examples is usually  $\sim 1.5C_{\text{fid}}$ .

### 2.3.4 Sedov Blast Wave

To test the forward evolution of our hydrodynamics solver in isolation we use the Sedov–von Neumann–Taylor (Von Neumann 1941; Sedov 1946; Taylor 1950) blast-wave (henceforth “Sedov”). The Sedov test is a rigorous and demanding evaluation for any three-dimensional Eulerian or Lagrangian hydrodynamic code. In this test, a simulation box is initialized with a uniform medium of constant density and negligible pressure. A concentrated source of thermal energy is introduced at the center at time  $t = 0$ . The main challenge lies in accurately simulating the strong spherical shock-wave that moves outward, sweeping material as it propagates through the surrounding medium. This setup is frequently used in astrophysics to model supernova explosions and the evolution of their remnants (Shu 1992; Blondin et al. 1998). A major advantage of the Sedov blast wave problem is that it can be solved analytically (Landau & Lifshitz 1987; Sedov 2018) and the solution has a self similar nature. The outward propagating shock in an ideal gas has radius

$$r_{sh}(t) = \phi_0 \left( \frac{E_0 t^2}{\rho_1} \right)^{1/5}, \quad (21)$$

where  $\phi_0 = 1.15$ .

In our example, we evolve the initial position and energy of a Sedov Blast to make observations of the late time density field. For our configuration, we use a box with  $128^3$  cells and constant initial

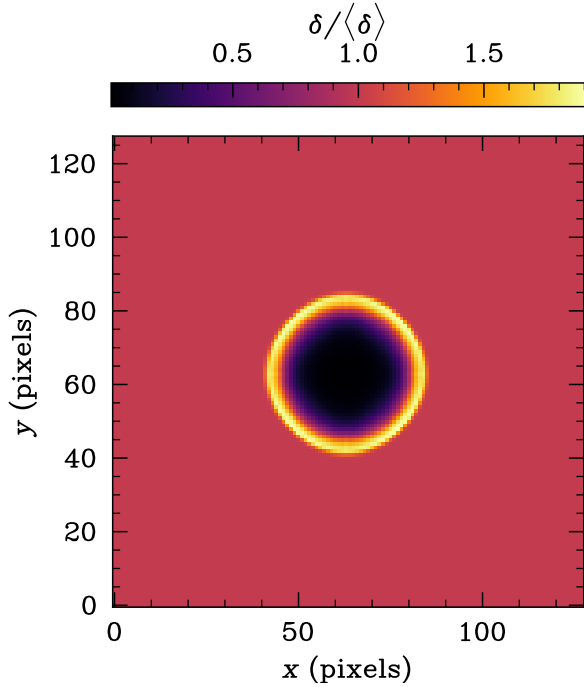


**Figure 1.** Central slice of a Sedov-Taylor blast-wave test conducted in a box with  $128^3$  cells after 30 time steps. Initial energy to density ratio tuned for the analytical radius to be  $r_{sh}(t_f) = 20.0$ .

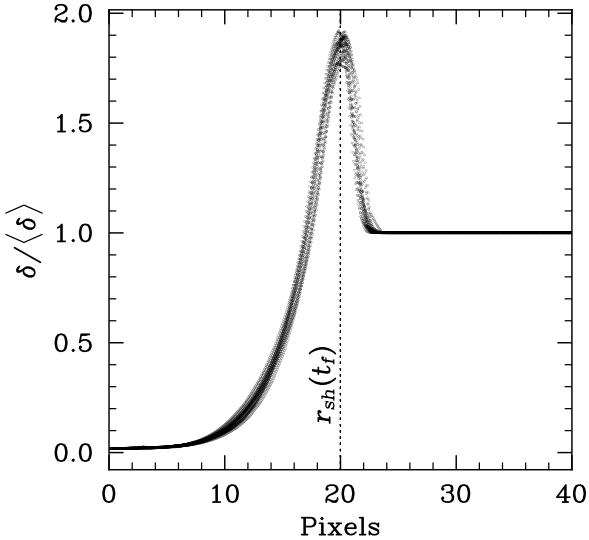


**Figure 2.** Density profiles at random angles from the center of the blast wave. Analytical radius from Eq. 21 shown.

density  $\rho_1 = 1$ . At the initial time,  $t = 0$ , we inject energy  $E_0$  into the central pixel of our grid. The simulation is stopped after thirty timesteps. We show the central slice through our blast wave in Figure 1, as well as the variation of the radial profile in Figure 2. We find our results in-line with the analytical prediction, with a shock-front well resolved within roughly 2 pixels, and angular variation of the shock profile of less than 1 pixel. These results are in line with other simulations of the Sedov blast, such as those in Trac & Pen (2003).

### 2.3.5 Implementation and Differentiation

Our code, `diffHydro` is written entirely in Python, allowing rapid development, while also utilizing JAX (Bradbury et al. 2021) for automatic differentiation and GPU-enabled computation. JAX provides familiar NumPy-like syntax while introducing powerful capabilities for gradient-based optimization, parallel computing, and just-in-time (JIT) compilation. This compilation is a computational technique that enables the conversion of Python functions into optimized machine code via the XLA (Accelerated Linear Algebra) compiler, enhancing computational efficiency on modern hardware. For cosmological hydrodynamical simulations, which require extensive numerical computations to model fluid dynamics and gravitational interactions across vast time steps and scales, JIT compilation offers substantial performance benefits. By reducing function call overhead and enabling optimizations such as loop fusion and vectorization, JIT compilation allows for more efficient utilization of GPUs. This efficiency can facilitate faster and more scalable simulations, enabling the high-fidelity modeling required for studying the evolution of cosmic structures.

The core innovation of JAX is its ability to automatically differentiate (Wengert 1964; Bartholomew-Biggs et al. 2000; Griewank & Walther 2008) through complex linear algebra operations and associated algorithms. This is achieved through its function `jax.grad`, which computes gradients of scalar-valued functions, and `jax.jacobian`, which computes full Jacobians. Unlike “traditional” autodiff libraries (such as TensorFlow) that maintain a computational graph during runtime, JAX adopts a “trace-and-transform” approach. It traces the Python function into a functional, stateless representation and then applies transformations like differentiation (`grad`), vectorization (`vmap`), and parallelization (`pmap`). This design makes JAX more composable and efficient for large-scale computations.<sup>1</sup>

JAX’s autodiff system is based on forward-mode and reverse-mode autodiff, with a focus on reverse-mode differentiation for most deep learning/high dimensional optimization applications. Reverse-mode autodiff is particularly efficient for scalar output functions with high-dimensional inputs, such as the loss function of field level inference problems. JAX accomplishes this by leveraging operator overloading, a technique where every mathematical operation is wrapped in a special “primitive” that tracks inputs, outputs, and computational rules. When `jax.grad` is applied, it “replays” these operations in reverse to compute gradients.

Unlike symbolic differentiation, which works with algebraic expressions, or finite differences, which approximates derivatives numerically, JAX operates directly on the computation’s underlying primitives. Each primitive corresponds to a low-level operation (like `add`, `multiply`, or `dot`), and JAX defines the derivatives for these primitives explicitly. As JAX traces the execution of a function, it records how these primitives are composed. During the backward pass, it uses the chain rule to propagate gradients from the output back to the inputs. This system enables efficient differentiation through linear algebra, such as the TVD numerical routine described above.

One concern with automatic differentiation with complex forward models is memory costs of the intermediate states and how to best

<sup>1</sup> In practice this trade-off involves a relatively lengthy compilation step once a model is built for function values and gradients, but very rapid function evaluation. For the applications shown in Sec. 3, the compilation time was approximately 10 minutes and evaluation was 10 seconds. This rapid evaluation is key for techniques like Hamiltonian Monte Carlo.

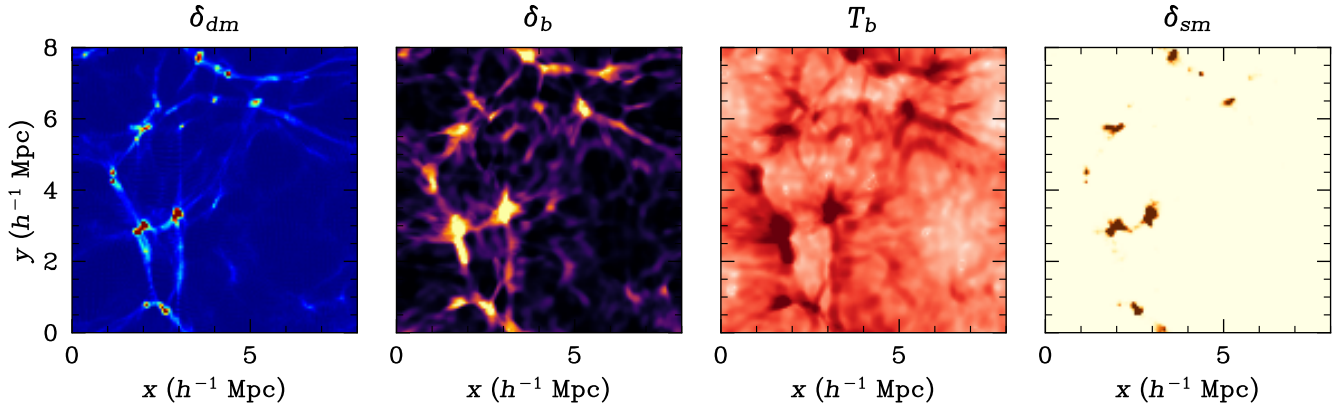


**Figure 3.** Example simulation in a  $256^3$  resolution box evolved to  $z = 2.5$ . Shown is the dark matter density field, baryon density field, temperature field, and the tracked star particles.

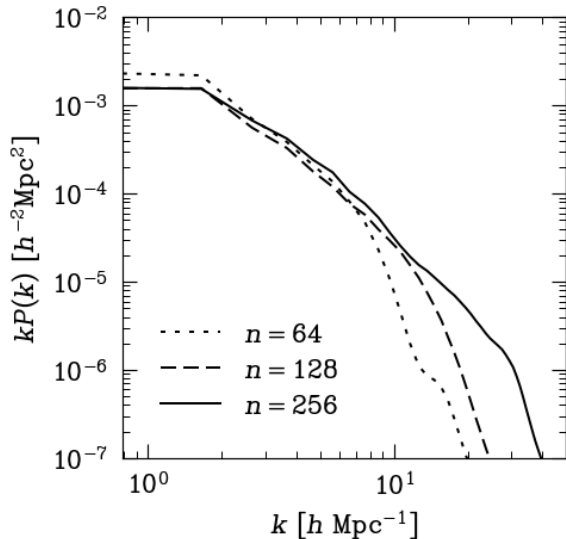


**Figure 4.** Convergence test of `diffHydro` (without sub-grid physics) for evolved baryon density field for an  $8 h^{-1}$  Mpc box at  $z = 2.5$ , changing box size while keeping the same initial conditions. We find excellent agreement even at relatively coarse resolutions up to  $k \sim 7.0 h \text{ Mpc}^{-1}$ .

balance memory usage and performance. JAX checkpointing is a tool that saves intermediate states (or “checkpoints”) of a computation, allowing JAX to recompute only certain parts of the computation graph during backpropagation, rather than holding the entire graph in memory. This trade-off reduces memory usage at the cost of additional computation time. This is particularly useful in recurrent computations or large transformations, where memory constraints are significant. By strategically placing checkpoints, one can control the balance between memory usage and computation overhead. In our case, we manually specify check-pointing every 6 time-steps, i.e. after every iteration of the Strang-splitting scheme, which strikes a good balance between memory and performance.

We show the performance of our model in Figure 4 up to a grid resolution  $256^3$ . The current code is a proof of concept and not currently parallelized to be deployed across multiple GPUs, so the forward pass is memory constrained. However, even at these modest resolutions we find consistent modeling well into the non-linear

regime. A full comparison to existing cosmological hydrodynamical simulations will be explored in future work with a parallelized implementation of `diffHydro`.

## 2.4 Subgrid Example: Star Formation and Energy Injection

There are many possible ways to include physics below the resolved physical scales, such as star formation and AGN activity, known as “sub-grid physics.” In this work we will focus on showing that a fairly simple stochastic subgrid-physics model which includes many features of those found in literature. In our current proof of concept, our resolution is not sufficient for full reproduction of the more complex aspects of these models which we leave for future work.

### 2.4.1 Toy Model

We focus on recreating a simplified version of the approach used in the IllustrisTNG/AREPO galaxy formation model (Springel & Hernquist 2003; Springel 2010; Vogelsberger et al. 2013; Genel et al. 2014; Weinberger et al. 2017; Pillepich et al. 2018; Weinberger et al. 2020), which is the basis of a large number of hydrodynamical simulation suites (Villaescusa-Navarro et al. 2021; Pakmor et al. 2023; Xu et al. 2023; Byrohl et al. 2024). This model is inspired by the Kennicutt–Schmidt law (Schmidt 1959; Kennicutt 1989) relating surface gas density and star formation rate.

In particular, we say there is some critical temperature,  $T_c$ , below which star formation is possible if a gas density criteria,  $\rho_c$ , is exceeded. The probability of formation is proportional to a rate density,  $\Pi_0$ . Since, in this work, we are primarily interested in the IGM physics as opposed to the stellar populations, we are primarily concerned with the effects of the resulting supernova heating on the gas. While in principle there is a delay between star formation events and their associated supernova, this scale is quite small relative to our timestepping, self-regulation establishes itself quickly, and the delay can be neglected. We assume that the supernovae feedback energy directly heats the surrounding gas density at an equivalent energy,  $E_0$ . In practice, this creates a Sedov-Taylor blast wave, which is a common model used for supernova studies (Blondin et al. 1998; Oku et al. 2022), and which we show in isolation without large scale structure and gravity in Sec. 2.3.4.

While relatively simplistic, this model contains many of the key features of a wide variety of sub-grid physics feedback models. In

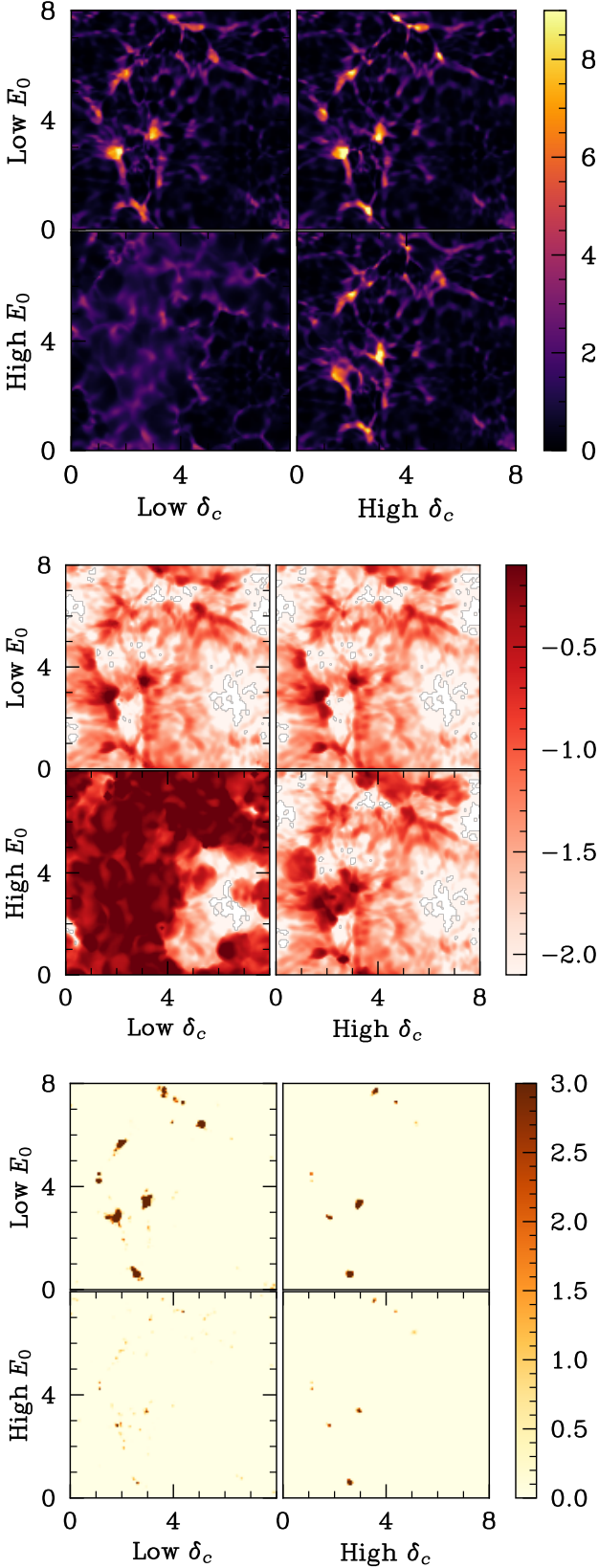


**Figure 5.** Demonstration on how baryon density, internal energy, and stellar field can change with varying the subgrid physics parameters  $\delta_c \in [0.5, 1.5]$  and  $E_0 \in [0.01, 0.05]$  with fixed initial conditions at  $z = 2.5$ . Slices are projected over a  $100 h^{-1}$  kpc thick slab.

particular it stochastically injects energy into the surrounding gas with some characteristic timescale. It is described by a relatively small number of parameters ( $T_c$ ,  $\rho_c$ ,  $\Pi_0$ , and  $E_0$ ) which can be tuned to reproduce various observed statistics. Since we do not currently have implemented the metal heating/cooling, we need to use a high value of  $T_c$  and/or a low value of the  $\delta_c$  to allow star formation, however star formation will self regulate with a sufficiently large  $E_0$  value.

Once star particles are created, we associate them with the nearby dark matter particles to track their future evolution. To do this we apply a cloud in cell readout routine to the 3d star field mesh at the dark matter particle positions. This provides a remapping from the Eulerian coordinate-defined stellar field to the dark matter particles. We then add this quantity to the dark matter particle’s auxiliary field variable. Currently this does not affect the resulting evolution and is used for diagnostic/plotting purpose only, however additional sub-grid physics prescriptions could be added for continued IGM heating.

We note that this approach differs from that in the standard AREPO galaxy formation models where new star particles are created and then evolved. However, once created both star particles and dark matter particles evolve as collision-less gravitationally interacting particles (i.e. via Eq. 1) and will have the same trajectories in phase space. Since, by construction, stars form in dense environments there will likely be a dark matter particle close to the formation zone and will be a suitable choice as a sample for the phase space evolution. Additional care may be needed to properly account for differences in gas and dark matter velocity depending on application.

We show one example including the star field in Figure 3. This box is evolved until  $z = 2.50$  and shows the dark matter field, the gas density, gas temperature, and stellar density field. As expected, we find the baryons trace the dark matter structures and the stellar field is a highly biased version of the baryon field.

We show examples of our varying our subgrid physics model in Figure 5, evolved to  $z = 2.0$ . In extreme cases, our feedback is able to completely overwhelm the gravitational binding energy and disrupt the baryon structure, an extreme analogy of a supernova event. At more reasonable levels of feedback, we find the expected result of heating the IGM in dense regions. As the critical density,  $\delta_c$  increases, we find less impact of our feedback since the large scale structure takes longer to evolve to this density and there will be fewer star formation events.

#### 2.4.2 Differentiation

Our goal is to compute gradients of any observable with respect to sub-grid physics parameters throughout the simulation. Conventional understanding suggests that differentiating through stochastically sampled discrete random variables, like the formation of an AGN or star cluster, is not feasible. However, advances in Reinforcement Learning have introduced techniques to handle such discrete variables in the training of deep neural networks via backpropagation.

Specifically, we apply the Gumbel-Softmax or CONCRETE method, which uses continuous distributions to approximate the sampling process of discrete stochastic variables, such as galaxies, in a differentiable manner (Jang et al. 2016; Maddison et al. 2016). This approach leverages two key insights: 1) a re-parameterization of a discrete (or categorical) distribution using the Gumbel distribution, and 2) making the corresponding function continuous by applying a continuous approximation controlled by a temperature parameter, which, at zero temperature, reduces to the original discontinuous form. This approach has been used to populate discrete galaxies into

halos (i.e. a halo occupancy distribution) to allow differentiation of galaxy power-spectra with respect to the HOD parameters (Horowitz et al. 2024).

The central concept of this technique, known more generally as the reparameterization trick, is to express samples  $z$  from a given parametric distribution  $\mathbb{P}_\theta$  as a deterministic, differentiable transformation  $f$  applied to a fixed distribution  $\mathbb{P}_\epsilon$ :

$$z = f(\theta, \epsilon) \quad \text{where} \quad \epsilon \sim \mathbb{P}_\epsilon \quad (22)$$

This reparameterization of the samples bypasses the need to differentiate the stochastic variable  $\epsilon$  when computing the derivatives of some downstream function  $h$  with respect to the distribution parameters  $\theta$ . This can be written in terms of the expectation with respect to the random variable  $\mathbb{E}_z$  as:

$$\frac{\partial}{\partial \theta} \mathbb{E}_{z \sim \mathbb{P}_\theta} [h(z)] = \mathbb{E}_{\epsilon \sim \mathbb{P}_\epsilon} \left[ \frac{\partial}{\partial \theta} h(f(\theta, \epsilon)) \right] \quad (23)$$

On the right-hand side of this equation, the derivative now only involves taking the gradient of a deterministic function of  $\theta$ , with  $\epsilon$  treated as an input to the function. While this can be used to construct real valued outputs, we need our mapping to be discrete (either star particle is formed, or not). We can then use the Gumbel trick (Gumbel 1954) combined with a softmax formula to construct an array  $z$  to describe the star forming field per timestep;

$$\hat{z} = \frac{\exp((\log(\pi_0) + g_0)/\tau)}{\exp((\log(\pi_0) + g_0)/\tau) + \exp((\log(1 - \pi_0) + g_1)/\tau)}, \quad (24)$$

where  $g_i$  are independent random variables drawn from the Gumbel distribution between 0 and 1, Gumbel(0, 1), which are treated as inputs to our model (see Eq. 23).

In the limit of  $\tau \rightarrow 0$ , Eq. 24 will exactly match the true discrete random field, however we can differentiate this formula in relation to the class probabilities  $\pi$  if  $\tau > 0$ . Care needs to be taken to maintain numerical accuracy, as very small values of  $\tau$  will result in significant noise due to the divisions of large numbers in Equation 24. In practice, trial and error is the most expedient way to choose  $\tau$  that results in the right stochastic properties while maintaining sufficient numerical accuracy (see Horowitz et al. (2024) for more discussion). For examples in this work, we found  $\tau = 0.1$  suitable.

In order to maintain smooth derivatives and improve general performance, we use a sigmoidal activation,  $\sigma(x) = (1 + \exp(-x))^{-1}$ , for the temperature and density thresholds instead of a sharp cutoffs. We define our class probability to be

$$\pi_0(\rho, T) = \Pi_0 \sigma\left(\frac{\delta - \delta_c}{a}\right) \sigma\left(\frac{T_c - T}{b}\right), \quad (25)$$

where  $a$  and  $b$  describe how sharp the transition is near the critical temperature. In the limit as  $a, b \rightarrow 0$  we recover the discontinuous transitions. In principle, these could be treated as additional sub-grid physics parameters and jointly fitted, but in this work we treat them as hyper-parameters (like  $\tau$ ) which are set at values to ensure numerical stability during backpropagation.

### 3 APPLICATIONS

In this section we highlight two applications of our differentiable framework;

- (i) Jointly sampling cosmology and subgrid physics from mock cosmological summary statistics
- (ii) Field level inference of initial matter density field given noisy mock observations

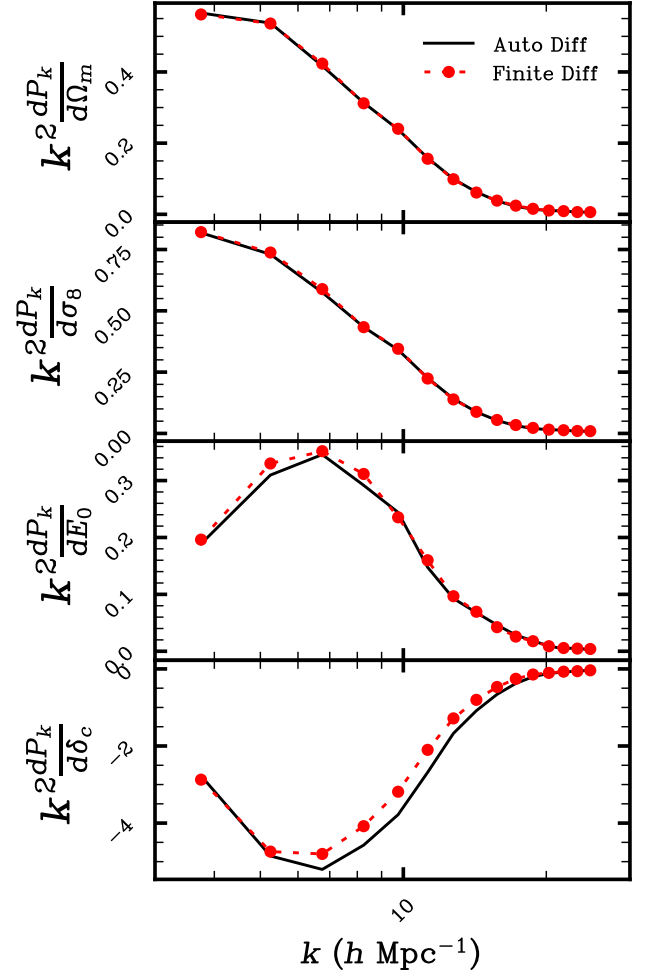


**Figure 6.** Comparison of our automatically calculated power spectra derivatives vs. those found via finite differences at  $z = 2.97$ . We perform our comparison at a fixed realization in order to show the accuracy of our derivative calculation. While methods are susceptible to numerical noise, downstream likelihood calculations aren't significantly effected. Note that at these cosmological values,  $dP_k/d\Omega_m$  and  $dP_k/d\sigma_8$  have very similar shapes, but their ratio does have a  $k$ -dependence.

#### 3.1 Joint Stochastic Subgrid and Cosmological Parameter Inference from Baryon Power Spectra

For our first example, we will construct a mock observation of the baryon density power spectra including sub-grid physics, and then infer posteriors on the associated parameters. A similar approach was taken in Lanziari et al. (2023) in the context of weak lensing analysis, where differentiability was used to construct rapid Fisher forecasts for various summary statistics. In our case, we will construct the entire posterior via Hamiltonian Monte Carlo sampling of the physical parameters.

We use our model including both baryons and dark matter to simulate a three dimensional volume. We use a particle grid resolution of  $128^3$ , a physical scale of  $8 h^{-1}$  Mpc, and evolve our field to  $z = 3.0$ .

We show the effect of varying these parameters on the power spectra in Figure 8. We study the joint inference of  $E_0$ ,  $\delta_c$ ,  $\sigma_8$ , and  $\Omega_m$ , holding all other parameters constant. These parameters are



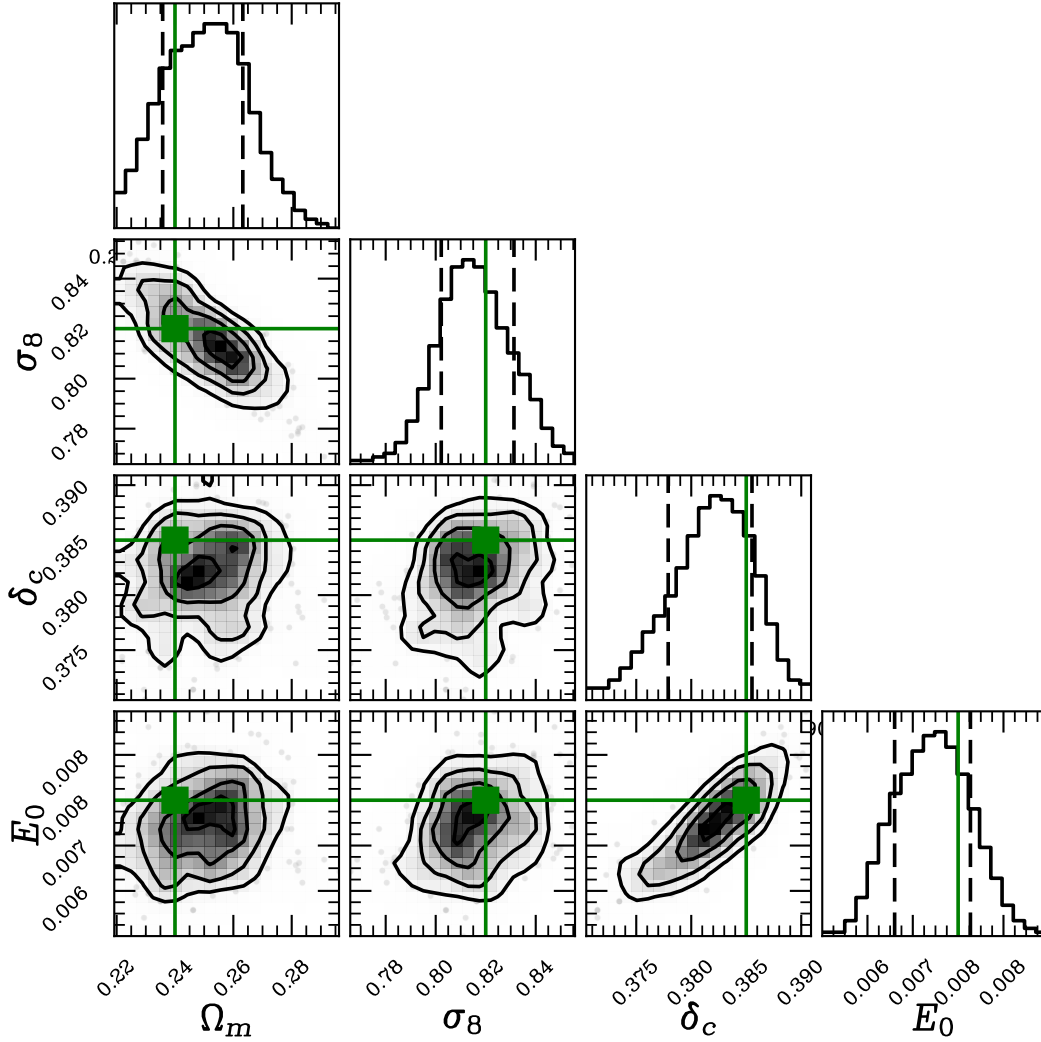


**Figure 7.** Hamiltonian Monte Carlo chain estimating the posterior for cosmological and astrophysical parameters given late-time baryon power spectra. The green point is the true simulated value, which is within one sigma of the estimated distribution mean for all four varied parameters.

chosen to be representative of both cosmology and sub-grid physics, while keeping the dimensionality small for demonstration.

To model a mock observation, we evolve our system using the methods described in Sec. 2.4, and calculate the power spectra of the baryon density using a differentiable routine described in (Horowitz et al. 2024). For our likelihood covariance, we run 100 boxes with independent initial seeds and use the full covariance of those boxes baryon power-spectra.

To test our differentiable framework, we show the automatic derivatives of our power spectra with respect to the parameters in Figure 6, compared with those calculated with finite differences. We find satisfactory accuracy across a range of scales. Also note that due to the accept-reject step of HMC, inaccurate derivatives will not necessarily lead to inaccurate posteriors but might reduce acceptance rate.

To evaluate the posteriors using our differentiable hydrocode, we sample over the joint subgrid physics and cosmological parameters using a Hamiltonian Monte Carlo (HMC) (Duane et al. 1987; Neal et al. 2011). We use the NoUTurn HMC implementation (Hoffman et al. 2014) in BlackJAX (Cabezas et al. 2024) to adaptively set our

step size. We use Gaussian priors on our parameters, centered at the true values, with  $\sigma = 0.002$  for  $E_0$  and  $\sigma = 0.02$  for  $\Omega_m/\sigma_8/\delta_c$ .

We use one chain initialized around our fiducial cosmological and hydrodynamical parameters with 500 steps (50 steps of burn-in). We found our sampler was able to generate negative autocorrelation, with chains having an effective sample size<sup>2</sup> of  $\sim 6600$ . We show the results of this chain in Figure 7. We find the well-known degeneracy in the  $\sigma_8$ - $\Omega_m$  plane, as well as a degeneracy in the  $\delta_c$ - $E_0$ . This latter degeneracy is due to the need for additional energy to compensate for a higher critical density, and therefore fewer possible star formations. Due to the small box size, we are unable to recover possible degeneracies between the sub-grid physics parameters and the cosmological parameters.

<sup>2</sup> The effective sample size can be calculated from a Markov chain as

$$N_{\text{eff}} = \frac{N}{1 + \sum_{t=1}^{\infty} \rho_t}, \quad (26)$$

where  $N$  is the number of samples and  $\rho_t$  is the autocorrelation of length  $t$ .

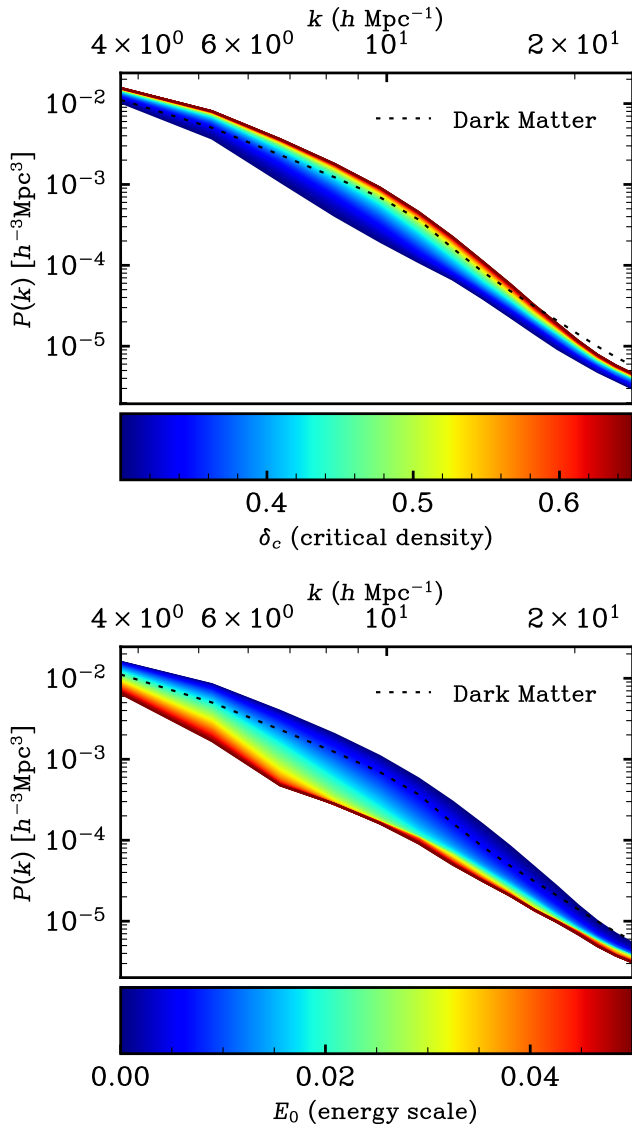


**Figure 8.** Effects of varying two sub-grid physics parameters at  $z = 2.97$  shown in relation to the dark matter power spectra at the fiducial parameters.

### 3.2 Field level inference

For our second example, we aim to reconstruct the full initial conditions corresponding to the observed volume. While in full generality these conditions should be sampled jointly with the model parameters, in this example will aim to reconstruct the conditions at fixed cosmology. In addition, for this example, we turn off the subgrid physics model to avoid having to jointly sample the stochastic field.

We construct a mock observable,  $\mathbf{d}$  that is proportional to gas-mass-weighted 3-dimensional temperature, i.e. a noisy measurement of  $\delta_b T$ . This corresponds roughly to the internal energy density of the field and is meant to represent a generic IGM/ICM probe. We apply Gaussian pixel noise with two different models. For our high S/N case, we apply noise with variance equal to the data variance, i.e.  $S/N = 1$ . For our low S/N case, we apply noise with 5 times the data variance, i.e.  $S/N = 5$ .

Following the approach in (Horowitz et al. 2019a, 2021), we perform an optimization to infer the initial conditions,  $\mathbf{s}$ , rather than sampling for computational expediency. In addition, in many cases

variations around an optimized solution can be used for constructing robust posteriors with far fewer function evaluations than full sampling (Horowitz et al. 2019b; Millea & Seljak 2022). Our log-posterior is the sum of a noise-weighted mean squared error over the pixels and a prior term, i.e.

$$\log \mathcal{L} = \frac{1}{2} \sum_i \left[ \frac{(d_i - F(\mathbf{s})_i)^2}{N_i} + |\tilde{s}_i|^2 \right], \quad (27)$$

where  $F$  is `diffHydro`,  $N_i$  is the variance of the pixel noise in the  $i$ th pixel. The second term is our prior, in this case we aim to minimize the initial phases,  $\tilde{\mathbf{s}}$  (i.e. the transfer function de-convolved initial conditions). Note that this second term is cosmological dependent, and we perform this optimization at our fiducial cosmology.

To optimize, we use the `optax` (DeepMind et al. 2020) implementation of the Limited-memory Broyden–Fletcher–Goldfarb–Shanno (L-BFGS) quasi-Newtonian method, with convergence criteria  $\epsilon = 10^{-5}$ . L-BFGS is an iterative algorithm designed for solving unconstrained optimization problems, particularly effective in high-dimensional spaces. It is a variant of the BFGS method that approximates the inverse Hessian matrix using a limited amount of memory, making it computationally efficient for large-scale problems. L-BFGS achieves this by storing only a few vectors past vectors (in our case  $M = 8$ ) that represent the gradient updates, avoiding the explicit computation and storage of the Hessian matrix. This property, combined with its fast convergence and ability to handle non-linear and differentiable functions, makes L-BFGS particularly suited for high-dimensional optimization tasks.

We show our qualitative results for the low S/N case in Figure 9 for both the reconstructed initial conditions and the expected target redshift energy density. Small scale modes are washed out due to the pixel noise in an analogous way as a Wiener Filter (e.g. Horowitz et al. (2019b)), however we are still able to reconstruct the large wavelength modes and recover the significant cosmic structure. Quantitatively, we can examine the reconstructions performance in terms of reconstructed power spectra and cross correlation coefficient. We show these quantities in Figure 10. The cross correlation coefficient is a measure of how well the actual phases of model are reconstructed as a function of scale, and can be written in terms of the auto and cross power spectra,  $P(k)$ , as

$$r_c(k) = \frac{P_{XY}(k)}{\sqrt{P_{XX}(k)P_{YY}(k)}}, \quad (28)$$

where  $X$  and  $Y$  are the reconstruction and model fields respectively. As expected, we find the higher signal mock provides a more accurate reconstruction across a range of scales, as well as a more accurate reconstructed power spectra.

## 4 CONCLUSIONS

In this work we have demonstrated a concept of a fully differentiable hydrodynamical simulation, applicable for a range of physical problems. Our approach solves the underlying Euler equations without emulation or other approximate techniques and allows for inclusion of a range of sub-grid physics prescriptions. We have demonstrated its applicability to both summary statistic based parameter inference and field-level reconstructions.

Below we list some possible extensions of our implementation of `diffHydro` as well as possible alternative approaches depending on application:

(i) *Fixed hydrodynamical grid:* The scales resolved in the current implementation are best suited towards modeling intergalactic

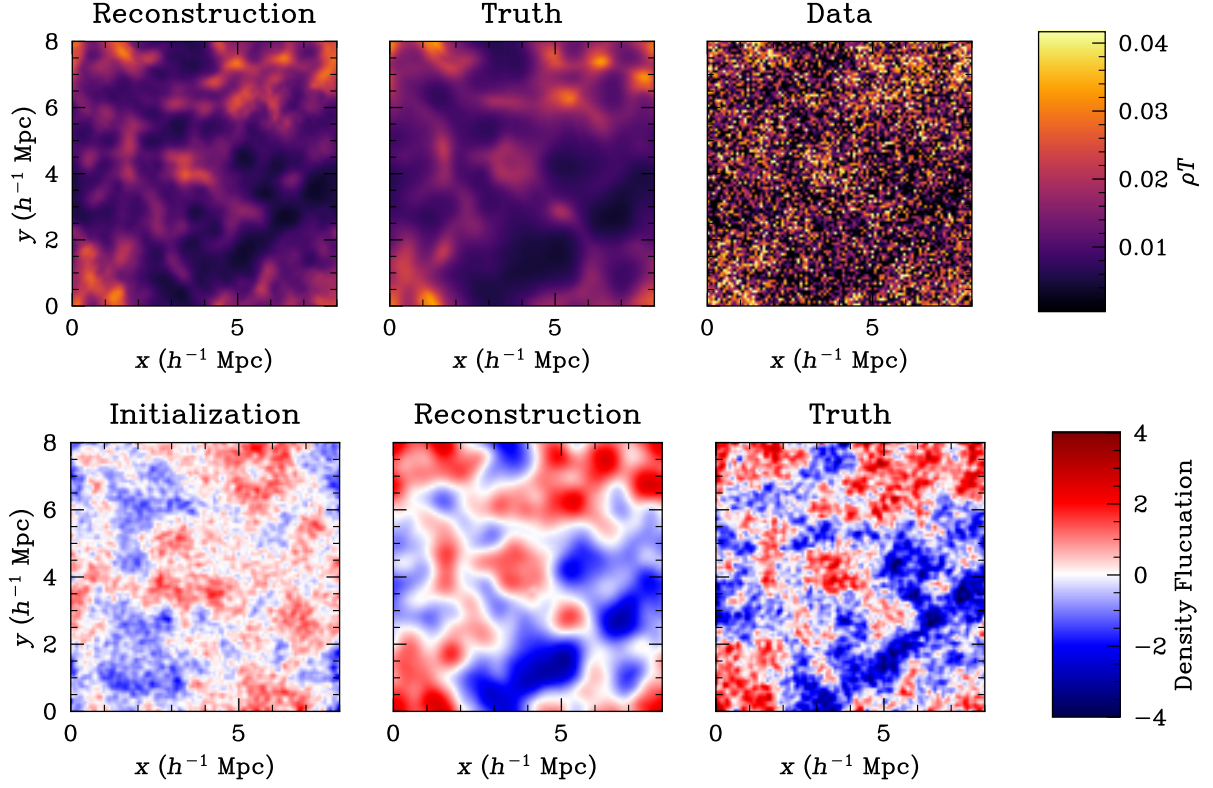


**Figure 9.** *Top:* Reconstruction of the late time internal energy field compared to the mock true field, with the data realization in the slice for comparison. *Bottom:* Reconstructed initial conditions compared to true initial condition. The initialization of the field is also shown to demonstrate our optimization started from a true random field.

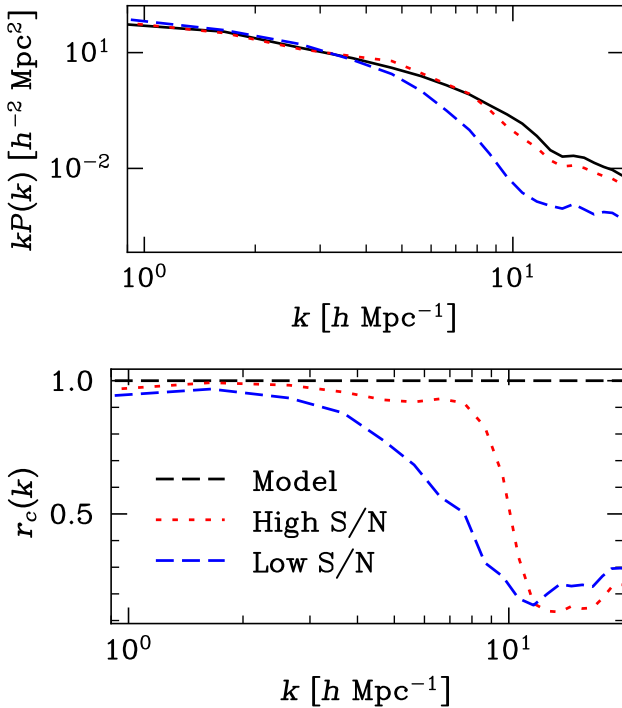


**Figure 10.** Powerspectra and cross correlation coefficient for our two mock samples compared to the simulated power spectra.

medium physics, with an eye toward understanding Ly- $\alpha$  absorption. This has allowed us to work at fixed grid scales since the IGM spans vast low-density volumes and is fully absorbed near to halos where adaptive methods would become relevant. Broadening the application of this work to other observables may require the implementation of adaptive mesh refinement (Truelove et al. 1998; Norman & Bryan 1999) and/or nested grid methods (Matsumoto & Hanawa 2003). Backpropagation through adaptive refinement methods would likely be challenging algorithmically due to the complex tree-structure that emerges. It may be sufficient to generate a refinement scheme on the forward pass, and use the same scheme during back-propagation, however this will likely increase numerical sensitivity as well as require recompilation of the model at each iteration.

(ii) *Dark matter particle dynamics:* Related to the fixed hydrodynamical grid is the use of fixed particle mesh dynamics instead of full n-body dynamics for the dark matter evolution. This may present serious issues in resolving galaxy-scale structures, and the full impact of this effect is dependent on the end-science case. Beyond the possible approaches discussed in Sec. 2.2, an exact strategy is the use of full n-body dynamics on the forward pass (i.e. running a standard hydrodynamical simulation) which will be used for the likelihood calculation, and then use `diffHydro` for derivative information for the update in the sampler.

(iii) *Memory limitations with back propagation:* Memory, for both the dark matter and baryonic fields, might become a significant limitation as the simulation resolution increases. In principle, one can also use adjoint based methods (i.e. PMWD, Li et al. (2024) for a particle mesh dark matter implementation), where back propagation is not used directly, but instead the gradients are propagated through

the adjoint solver. While the Euler equations are well known to admit an adjoint solution (Jameson 1988), in our context it also requires an adjoint equation for the sub-grid physics (see Sec. 2.4), which may be impossible depending on their construction.

(iv) *Parallelization across GPUs*: Currently, our implementation is on a single GPU, which limits the effective resolution and/or time-range in which we can model. The core TVD scheme for gas physics (Sec. 2.3) is straightforward to parallelize across GPU by splitting up the volume across the GPUs. Communication between the GPUs will be limited to the boundaries by construction. However, gravitational dynamics are currently implemented via a mesh method requiring fast Fourier transformations over the entire volume. While distributing FFTs across multiple GPUs is not itself a fundamental limitation (Gholami et al. 2015; Romero et al. 2022), extra care is needed to ensure proper backpropagation in a compiled JAX environment.<sup>3</sup>

(v) *Mapping to observables*: For this work, we study quantities that are direct functions of the baryon density and temperature field. In general, additional steps are required to map to actual observables. For example, Lyman- $\alpha$  Forest is modeled by including a thermionization model, an absorption profile, and an integration along the line of sight including redshift space distortions. While these sorts of complex physical processes can be included in a differentiable way (Ding et al. 2024), for the purpose of clarity we have just used the base simulation outputs and their corresponding power spectra. Other observables common in astrophysics, such as cluster counts and other observables which rely on discrete assignment, may present theoretical challenges in implementing within a end-to-end differentiable framework.

The novel approach of `diffHydro` allows a range of additional applications for cosmological and astrophysical inference beyond that available to traditional techniques. Possible applications include:

(i) *Improving fidelity with machine learning methods*: Differentiable cosmological hydrodynamical simulation allows the implementation of various machine learning-based refinement strategies for physical simulations. For example, “solver-in-the-loop” methods integrate deep learning augmentation at each time-step to refine the solution (Um et al. 2020). One can also apply deep learning models afterwards for refinement of relatively coarse (un-converged) simulations (Jacobus et al. 2023, 2024) or constrained generation of additional fields (Horowitz et al. 2022) at each time-step.

(ii) *High dimensional sub-grid physics inference*: Differentiable hydrodynamical simulation opens the door to implementing more expressive sub-grid physics via neural network models. Network parameters can be trained based on actual data by backpropagation through both the neural network and the simulation simultaneously. This would enable very expressive sub-grid models which could include history information (i.e. previous time-slice states) and non-local information. These sorts of hybrid end-to-end “online” training techniques have been used recently for Earth weather forecasting (Kochkov et al. 2024). These methods could further be employed as a model-independent search for new physics.

(iii) *Numerical scheme for gas evolution*: As additional physics are added and/or resolution is increased, the numerical sensitivity of solving our equations increases due to range of time scales involved. In this regime, it may be important to go beyond our explicit hydrodynamics solver and use implicit techniques. It is straightforward to implement implicit equation solving within JAX since the Jaco-

bian information can be computed via automatic differentiation (see Kidger (2021) as well as earlier Julia implementations (Rackauckas & Nie 2017)). This approach was used to solve the Einstein-Boltzmann equations in Hahn et al. (2024) and Li et al. (2023), and could be extended to the physics studied here.

(iv) *Expansion to ISM/ICM physics*: The techniques developed in this work for cosmological hydrodynamical simulations could also be applied to smaller-scale simulations of the interstellar medium or intra-cluster medium. Physics in existing codes, such as Athena (Stone et al. 2008; Stone et al. 2020) (magnetohydrodynamics), HARM (Gammie et al. 2003) (relativistic corrections), or FLASH (Fryxell et al. 2000) (stellar reactions) could be implemented within this framework. Insights from these small-scale simulations could also be used to infer physics at cosmological scales (Oku et al. 2022; Oku & Nagamine 2024), possibly within a single inference pipeline. Modeling these effects are a key component of upcoming and ongoing IGM/ICM surveys at both low (Lee et al. 2022; Khrykin et al. 2024) and high redshifts (Greene et al. 2022).

## ACKNOWLEDGEMENTS

We thank Khee-Gan Lee, Kentaro Nagamine, Peter Behroozi, Jamie Sullivan, Philip Mocz and Yuri Oku for their helpful insights and comments.

This research used resources of the National Energy Research Scientific Computing Center, a DOE Office of Science User Facility supported by the Office of Science of the U.S. Department of Energy under Contract No. DEC02-05CH11231.

## REFERENCES

- Aricò G., Angulo R. E., Contreras S., Ondaro-Mallea L., Pellejero-Ibañez M., Zennaro M., Stücker J., 2023, *baconemu: Cosmological emulators for large-scale structure statistics*, *Astrophysics Source Code Library*, record ascl:2307.010
- Ata M., Lee K.-G., Vecchia C. D., Kitaura F.-S., Cucciati O., Lemaux B. C., Kashino D., Müller T., 2022, *Nature Astronomy*, **6**, 857
- Ataei M., Salehipour H., 2024, *Computer Physics Communications*, **300**, 109187
- Bagla J. S., 2002, *Journal of Astrophysics and Astronomy*, **23**, 185
- Barnes J., Hut P., 1986, *Nature*, **324**, 446
- Bartholomew-Biggs M., Brown S., Christianson B., Dixon L., 2000, *Journal of Computational and Applied Mathematics*, **124**, 171
- Berthet Q., Blondel M., Teboul O., Cuturi M., Vert J.-P., Bach F., 2020, in *Proceedings of the 34th International Conference on Neural Information Processing Systems. NIPS '20*. Curran Associates Inc., Red Hook, NY, USA
- Blondin J. M., Wright E. B., Borkowski K. J., Reynolds S. P., 1998, *The Astrophysical Journal*, **500**, 342
- Bradbury J., et al., 2021, *JAX: Autograd and XLA*, *Astrophysics Source Code Library*, record ascl:2111.002
- Byrohl C., Nelson D., Horowitz B., Lee K.-G., Pillepich A., 2024, *arXiv e-prints*, p. arXiv:2409.19047
- Cabezas A., Corenflos A., Lao J., Louf R., 2024, *BlackJAX: Composable Bayesian inference in JAX* (arXiv:2402.10797)
- Campagne J.-E., et al., 2023, *The Open Journal of Astrophysics*, **6**, 15
- Cen R., 1992, *ApJS*, **78**, 341
- Chen T., Fox E., Guestrin C., 2014, in *International conference on machine learning*. pp 1683–1691
- Citrin J., et al., 2024, arXiv preprint arXiv:2406.06718
- Couchman H. M. P., 1991, *ApJ*, **368**, L23
- Dai B., Feng Y., Seljak U., 2018, *J. Cosmology Astropart. Phys.*, **2018**, 009

<sup>3</sup> For one possible approach to GPU distributed FFT in JAX, see <https://github.com/DifferentiableUniverseInitiative/jaxDecomp>.

- DeepMind et al., 2020, The DeepMind JAX Ecosystem, <http://github.com/google-deeppmind>
- Dimonte G., Tipton R., 2006, *Physics of Fluids*, **18**, 085101
- Ding J., Horowitz B., Lukić Z., 2024, *Astronomy and Computing*, **48**, 100858
- Dong C., Lee K.-G., Ata M., Horowitz B., Momose R., 2023, *ApJ*, **945**, L28
- Dong C., Lee K.-G., Cui W., Davé R., Sorini D., 2024, *MNRAS*, **532**, 4876
- Duane S., Kennedy A. D., Pendleton B. J., Roweth D., 1987, *Physics Letters B*, **195**, 216
- Eisenstein D. J., Hu W., 1998, *ApJ*, **496**, 605
- Eisenstein D. J., Hu W., 1999, *ApJ*, **511**, 5
- Feng Y., Chu M.-Y., Seljak U., McDonald P., 2016, *MNRAS*, **463**, 2273
- Fryxell B., et al., 2000, *ApJS*, **131**, 273
- Gammie C. F., McKinney J. C., Tóth G., 2003, *ApJ*, **589**, 444
- Genel S., et al., 2014, *MNRAS*, **445**, 175
- Gholami A., Hill J., Malhotra D., Biros G., 2015, *arXiv e-prints*, p. [arXiv:1506.07933](https://arxiv.org/abs/1506.07933)
- Giri S. K., Schneider A., 2021, *J. Cosmology Astropart. Phys.*, **2021**, 046
- Greene J., Bezanson R., Ouchi M., Silverman J., the PFS Galaxy Evolution Working Group 2022, *arXiv e-prints*, p. [arXiv:2206.14908](https://arxiv.org/abs/2206.14908)
- Griewank A., Walther A., 2008, Evaluating derivatives: principles and techniques of algorithmic differentiation. SIAM
- Gumbel E. J., 1954, Statistical theory of extreme values and some practical applications: a series of lectures. 0 Vol. 33, US Government Printing Office
- Habib S., et al., 2016, *New Astron.*, **42**, 49
- Hahn O., List F., Porqueres N., 2024, *J. Cosmology Astropart. Phys.*, **2024**, 063
- Harrington P., Mustafa M., Dornfest M., Horowitz B., Lukić Z., 2022, *ApJ*, **929**, 160
- Harten A., 1997, *Journal of Computational Physics*, **135**, 260
- Heitmann K., White M., Wagner C., Habib S., Higdon D., 2010, *ApJ*, **715**, 104
- Hirsch C., 1990, Chichester
- Hockney R. W., Eastwood J. W., 1988, Computer simulation using particles. Routledge
- Hoffman M. D., Gelman A., et al., 2014, *J. Mach. Learn. Res.*, **15**, 1593
- Horowitz B., Lee K.-G., White M., Krolewski A., Ata M., 2019a, *ApJ*, **887**, 61
- Horowitz B., Seljak U., Aslanyan G., 2019b, *J. Cosmology Astropart. Phys.*, **2019**, 035
- Horowitz B., Zhang B., Lee K.-G., Kooistra R., 2021, *ApJ*, **906**, 110
- Horowitz B., Dornfest M., Lukić Z., Harrington P., 2022, *ApJ*, **941**, 42
- Horowitz B., Hahn C., Lanusse F., Modi C., Ferraro S., 2024, *MNRAS*, **529**, 2473
- Jacobus C., Harrington P., Lukić Z., 2023, *ApJ*, **958**, 21
- Jacobus C., Chabanier S., Harrington P., Emberson J., Lukić Z., Habib S., 2024, *arXiv e-prints*, p. [arXiv:2411.16920](https://arxiv.org/abs/2411.16920)
- Jameson A., 1988, *Journal of scientific computing*, **3**, 233
- Jang E., Gu S., Poole B., 2016, *arXiv e-prints*, p. [arXiv:1611.01144](https://arxiv.org/abs/1611.01144)
- Jasche J., Wandelt B. D., 2013, *MNRAS*, **432**, 894
- Jin S., Xin Z., 1995, *Communications on pure and applied mathematics*, **48**, 235
- Kennicutt Robert C. J., 1989, *ApJ*, **344**, 685
- Khrykin I. S., et al., 2024, *ApJ*, **973**, 151
- Kidger P., 2021, PhD thesis, University of Oxford
- Kochkov D., et al., 2024, *Nature*, **632**, 1060
- Kooistra R., Lee K.-G., Horowitz B., 2022, *ApJ*, **938**, 123
- Kugel R., et al., 2023, *MNRAS*, **526**, 6103
- Landau L. D., Lifshitz E. M., 1987, *Fluid Mechanics: Volume 6*. Elsevier
- Laney C. B., 1998, *Computational Gasdynamics*. Cambridge University Press
- Lanzieri D., Lanusse F., Starck J.-L., 2022, in *Machine Learning for Astrophysics*. p. 60 ([arXiv:2207.05509](https://arxiv.org/abs/2207.05509)), doi:10.48550/arXiv.2207.05509
- Lanzieri D., Lanusse F., Modi C., Horowitz B., Harnois-Déraps J., Starck J.-L., LSST Dark Energy Science Collaboration (LSST DESC) 2023, *A&A*, **679**, A61
- LeVeque R. J., 2002, *Finite Volume Methods for Hyperbolic Problems*. Cambridge Texts in Applied Mathematics, Cambridge University Press
- Lee K.-G., Ata M., Khrykin I. S., Huang Y., Prochaska J. X., Cooke J., Zhang J., Batten A., 2022, *ApJ*, **928**, 9
- Lesgourgues J., 2011, *arXiv e-prints*, p. [arXiv:1104.2932](https://arxiv.org/abs/1104.2932)
- Lewis A., Challinor A., 2011, CAMB: Code for Anisotropies in the Microwave Background, Astrophysics Source Code Library, record ascl:1102.026
- Li Y., et al., 2022, *arXiv e-prints*, p. [arXiv:2211.09958](https://arxiv.org/abs/2211.09958)
- Li Z., Sullivan J., Millea M., 2023, *zackli/Bolt.jl: citation*, doi:10.5281/zenodo.10065126
- Li Y., Modi C., Jamieson D., Zhang Y., Lu L., Feng Y., Lanusse F., Greengard L., 2024, *ApJS*, **270**, 36
- Maddison C. J., Mnih A., Whye Teh Y., 2016, *arXiv e-prints*, p. [arXiv:1611.00712](https://arxiv.org/abs/1611.00712)
- Matsumoto T., Hanawa T., 2003, *The Astrophysical Journal*, **583**, 296
- Millea M., Seljak U., 2022, *Phys. Rev. D*, **105**, 103531
- Modi C., Feng Y., Seljak U., 2018, *J. Cosmology Astropart. Phys.*, **2018**, 028
- Neal R. M., et al., 2011, *Handbook of markov chain monte carlo*, **2**, 2
- Nguyen N.-M., Schmidt F., Tucci B., Reinecke M., Kostić A., 2024, *arXiv e-prints*, p. [arXiv:2403.03220](https://arxiv.org/abs/2403.03220)
- Norman M. L., Bryan G. L., 1999, in *Numerical Astrophysics: Proceedings of the International Conference on Numerical Astrophysics 1998 (NAP98)*, held at the National Olympic Memorial Youth Center, Tokyo, Japan, March 10–13, 1998. pp 19–28
- Oku Y., Nagamine K., 2024, *ApJ*, **975**, 183
- Oku Y., Tomida K., Nagamine K., Shimizu I., Cen R., 2022, *ApJS*, **262**, 9
- Pakmor R., et al., 2023, *MNRAS*, **524**, 2539
- Payot N., Lemos P., Perreault-Levasseur L., Cuesta-Lazaro C., Modi C., Hezaveh Y., 2023, *arXiv e-prints*, p. [arXiv:2311.18017](https://arxiv.org/abs/2311.18017)
- Pen U.-L., 1998, *ApJS*, **115**, 19
- Pillepich A., et al., 2018, *MNRAS*, **473**, 4077
- Planck Collaboration et al., 2020, *A&A*, **641**, A6
- Quinn T., Katz N., Stadel J., Lake G., 1997, *arXiv e-prints*, pp [astro-ph/9710043](https://arxiv.org/abs/astro-ph/9710043)
- Rackauckas C., Nie Q., 2017, *Journal of Open Research Software*, **5**, 15
- Rahimi A., Kawata D., 2012, *MNRAS*, **422**, 2609
- Robertson B. E., Kravtsov A. V., 2008, *ApJ*, **680**, 1083
- Romero J., Costa P., Fatica M., 2022, in *Proceedings of the Platform for Advanced Scientific Computing Conference. PASC '22*. Association for Computing Machinery, New York, NY, USA, doi:10.1145/3539781.3539797, <https://doi.org/10.1145/3539781.3539797>
- Schmidt M., 1959, *ApJ*, **129**, 243
- Schneider E. E., Robertson B. E., 2015, *ApJS*, **217**, 24
- Sedov L. I., 1946, *Journal of Applied Mathematics and Mechanics*, **10**, 241
- Sedov L. I., 2018, *Similarity and dimensional methods in mechanics*. CRC press
- Seljak U., Aslanyan G., Feng Y., Modi C., 2017, *J. Cosmology Astropart. Phys.*, **2017**, 009
- Sharma D., Dai B., Villaescusa-Navarro F., Seljak U., 2024, *arXiv e-prints*, p. [arXiv:2401.15891](https://arxiv.org/abs/2401.15891)
- Shu C.-W., 1988, *SIAM Journal on Scientific and Statistical Computing*, **9**, 1073
- Shu F. H., 1992, *The physics of astrophysics. Volume II: Gas dynamics*. University Science books
- Springel V., 2010, *MNRAS*, **401**, 791
- Springel V., Hernquist L., 2003, *MNRAS*, **339**, 289
- Springel V., Yoshida N., White S. D. M., 2001, *New Astron.*, **6**, 79
- Stone J. M., Gardiner T. A., Teuben P., Hawley J. F., Simon J. B., 2008, *ApJS*, **178**, 137
- Stone J. M., Tomida K., White C. J., Felker K. G., 2020, *The Astrophysical Journal Supplement Series*, **249**, 4
- Strang G., 1968, *SIAM journal on numerical analysis*, **5**, 506
- Taylor G., 1950, *Proceedings of the Royal Society of London Series A*, **201**, 159
- Teyssier R., Pontzen A., Dubois Y., Read J. I., 2013, *MNRAS*, **429**, 3068
- Trac H., Pen U.-L., 2003, *PASP*, **115**, 303
- Truelove J. K., Klein R. I., McKee C. F., Holliman II J. H., Howell L. H.,

- Greenough J. A., Woods D. T., 1998, *The Astrophysical Journal*, 495, 821
- Um K., Brand R., Yun Fei Holl P., Thuerey N., 2020, [arXiv e-prints](#), p. [arXiv:2007.00016](#)
- Van Leer B., 1974, *Journal of computational physics*, 14, 361
- Villaescusa-Navarro F., et al., 2021, [ApJ](#), 915, 71
- Vogelsberger M., Genel S., Sijacki D., Torrey P., Springel V., Hernquist L., 2013, [MNRAS](#), 436, 3031
- Von Neumann J., 1941, *Bethe [Bet47]*, p. 13
- Walther M., Oñorbe J., Hennawi J. F., Lukić Z., 2019, [ApJ](#), 872, 13
- Weinberger R., et al., 2017, [MNRAS](#), 465, 3291
- Weinberger R., Springel V., Pakmor R., 2020, [ApJS](#), 248, 32
- Wengert R. E., 1964, *Communications of the ACM*, 7, 463
- Xu C., et al., 2023, [MNRAS](#), 521, 4356